(Received 13 August 2024, Accepted 2 October 2024, Scheduled 6 November 2024)

Design of Multiband Metasurface Radome for Leading Wing Edge of Aircraft

Kanathil M. Arya[1, 2, *], Akshay M. Aserkar[3], Shailesh A. Patil[1], Raveendranath U. Nair[1], and Shiv Narayan[1]

[1] *CSIR — National Aerospace Laboratories, Bangalore, India*
[2] *Academy of Scientific and Innovative Research (AcSIR), Ghaziabad, India*
[3] *Birla Institute of Technology and Science, Pilani, India*

ABSTRACT: A novel metamaterial-element based frequency selective surface (FSS) is proposed in this paper for multiband radome for airborne application, which exhibits angular stability and polarization independence up to incidence angle, 60°. The proposed metasurface radome consists of a combination of different patch-type elements in two cascaded layers, forming an electrically thin design suitable for aerospace applications. It operates in the frequency bands, S- (3.3 GHz), C- (4.8 GHz), and X- (9.1 GHz) with high transmission efficiency and good isolation between bands (< -20 dB). An equivalent circuit model of the proposed design is derived and validated with the simulated (based on HFSS) and measured results. Further, a multilayered planar laminate is designed using the proposed metamaterial-element based FSS that exhibits transmission bandwidths, 220 MHz, 1 GHz, and 1.3 GHz corresponding to S-, C-, and X-bands, respectively, w.r.t -1 dB insertion loss. The structural analysis of multilayered radome wall configuration confirms its suitability for shared aperture antenna integrated to leading wing structure of aircraft.

1. INTRODUCTION

Radomes are protective structures placed over antennas to protect them from the environmental conditions and can withstand against aerodynamic loads, while being transparent to electromagnetic (EM) waves and not causing much degradation of the antenna performance. Depending on the application of the antenna, radomes are designed to perform additional functions apart from structural protection, such as enhancing gain and directivity, filtering out-of-band frequencies, and reducing radar cross section. In general, radomes are designed specifically for the given antenna. A shared-aperture antenna is one that operates at multiple frequency bands using only one aperture from a single location [1]. Such antennas are currently desirable for aerospace applications due to space constraints onboard aircraft. The primary design requirement for a radome for shared aperture antenna is that of multiband operation corresponding to the multiple operating frequencies of the antenna. Multiband filtering characteristics can be imparted to a radome using a frequency selective surface (FSS)-based design.

Frequency selective surfaces are periodic structures that act as spatial filter for EM waves impinging on it and have widespread applications such as radar absorbing structures, reflector antennas, and radomes [2]. An FSS can be embedded in a radome wall to provide advanced functions like filtering with sharp roll-off characteristics. Depending on the filter characteristics of the FSS, it can be classified as single-band, dual-band, or multiband FSS [3, 4]. The design in [5] shows single band operation, and it uses cascaded resonant elements to place multiple transmission zeros and poles. This creates a band pass with two wide stopbands on either side. During FSS design, it is beneficial to have a reliable method of tuning the transmission null to a specific frequency, so that a required characteristic can be achieved without relying completely on a trial-based approach. A method has been explained in [6] for the tuning of transmission null using an equivalent circuit model (ECM) approach. Similar methods have been used to achieve dual-band characteristics in [7], using a convoluted hybrid resonator. Later, stable dual-band behavior is also demonstrated in [8] and [9]. A procedure to combine different elements to tune multiple poles and zeros, thus achieving a multiband response, has been proposed in [10]. Multiband FSS designs can be achieved in different ways, including the combination of multiple resonant elements on a single layer, cascading different FSS layers, using self-repeating or fractal elements, etc. [11]. Further, four passbands have been achieved in [12] by meandering an FSS structure. Multiband performance has been achieved in [13] using LC resonators to model and optimize the design. The development of an FSS-based radome requires an angular stable and polarization independent FSS structure, which enables the realization of conformal FSS-radome. This is especially important for aerospace applications, where the spatial orientation of the aircraft varies constantly. Angular stability has been achieved using various different designs for different polarizations [5, 6, 12]. In general, increasing packing fraction of the unit cell and its symmetry aids in angular stability. However, it is more difficult to achieve stability for multiband FSS

* Corresponding author: Kanathil Meethal Arya (aryakm@nal.res.in).

structure because of the interaction between different elements and the effect of grating lobes.

The 2-D metamaterial structures known as metasurfaces (MTSs) offer several advantages over FSS structures, including low profile, elimination of grating lobes in reflected and transmitted fields, minimal absorption, and cost-effectiveness [14]. In open literature, most MTS-based radomes primarily focus on radar cross-section (RCS) reduction, gain enhancement, and absorption [15–17]. Also, both MTS and a combination of MTS and FSS-based designs can lead to the development of high-efficiency transmission radomes, as reported in [18–20]. However, all of these structures demonstrate angular stable performance over a single frequency band. In this work, a novel MTS design is proposed that consists of the combination of elements on a single layer and cascading with the MTS-elements printed on another side of the same substrate to achieve a highly stable response till 60° of oblique incidence. It is an improvement over previously reported multiband designs due to its simple structure, having only two MTS layers and a very thin layer of substrate ($\lambda/30$ w.r.t highest operating frequency). Moreover, it uses a combination of very basic FSS elements such as Jerusalem cross and square loop that are easier to model and analyze. The proposed metasurface structure is highly stable at three resonant frequencies, viz. 3.3 GHz, 4.8 GHz, and 9.1 GHz associated with S-, C-, and X-bands, respectively, which are not served by previously designed structures. This work is already reported by authors in [21]. Here again it is presented to study its metamaterial behavior, ECM model, and its practical application in detail. The present paper is organized as follows. Section 2 describes the details of the geometry of metasurface unit cell of proposed MTS along with its design procedure and operating principle. The derivation of ECM of the proposed design and its validation with the simulated results are presented in Section 3. Section 4 describes the prototype development and EM measurement of the designed MTS. In Section 5, the MTS based multi-layered planar radome wall configuration has been presented. Further, structural analysis of the proposed design is presented in Section 6 in view of aerospace applications. Finally, Section 7 draws the conclusion of the proposed work.

2. DESIGN OF FSS AND OPERATING PRINCIPLE

2.1. Metasurface Unit Cell Structure

The topology of the proposed MTS unit cell is illustrated in Fig. 1. It is composed of two different layers of MTS elements termed as MTS Layer-I & -II, separated by a Glass epoxy substrate ($\varepsilon_r = 4.27$ and loss tangent, $\tan\delta = 0.016$) of thickness, $h2 = 0.508$ mm. An additional layer of Glass epoxy of the same thickness covers the MTS layer (thickness, $h = 0.035$ mm) on the upper side. This will protect the outer surface of the MTS structure which is exposed to the outside environment. The inner side is left uncovered. This approach minimizes the thickness of the MTS structure and maximizes the transmission, while ensuring that the radome wall is structurally durable and resistant to erosion. The metallic elements in the MTS layers consist of patch type structures such as Jerusalem cross (JC), gridded square loop, and cross-shaped loop. At the upper side of substrate (MTS Layer-I), each unit cell is composed of a JC surrounded by a gridded square loop. The length of the square grid is the same as that of the periodicity ($p = 15.5$ mm) of the unit cell. The bottom side of the substrate (MTS Layer-II) also contains JC, but it is positioned at the corners of the unit cell. As a result, even though the two JC arrays are cascaded, they do not directly overlap, which reduces the coupling effects that would result from positioning one directly over the other, making it more angular stable. To suppress the power transmission in higher frequency side (beyond X-band), a small cross-shaped loop is incorporated in the center of the lower layer, which introduces a wide transmission null. Since the structure is symmetrical in two perpendicular directions (x- and y-axes), it ensures polarization independence. While designing the proposed MTS unit cell, the periodicity has been kept as small as possible; the width of the metallic elements is minimized; and the amount of empty space between patch type elements is reduced. This forms a compact unit cell and contributes to its angular stability by reducing the effect of grating lobes. The schematics of both the layers of MTS unit cell are shown in Fig. 2 along with the dimension details. The optimized dimensions for the proposed design are specified in Table 1.

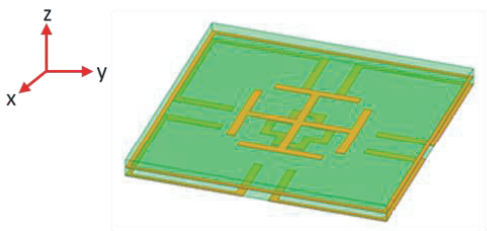

FIGURE 1. Unit cell structure of proposed MTS.

TABLE 1. Optimized design parameters of MTS.

	Design parameters	Values(mm)
MTS Layer- I	l_1	6.0
	l_2	5.0
	w_1	0.5
	w_2	0.25
MTS Layer-II	l_3	6.25
	l_4	3.5
	l_5	1.0
	w_3, w_5	0.25
	w_4	0.5

To investigate the metamaterial behavior of the proposed multiband MTS structure, the values of effective permeability and permittivity have been retrieved from the simulated transmission and reflection coefficients, using Kramers-Kronig relations [20, 22]. The structure is observed to exhibit negative permittivity and permeability over the operating frequency range, 1–11 GHz (see Fig. 3). Thus, the proposed multi-layered structure shows metamaterial behavior over the desired frequency bands and hence termed as metasurface.

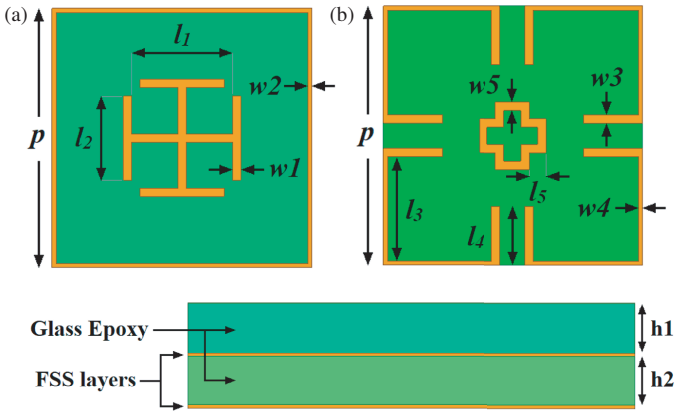

FIGURE 2. Schematic of unit cell with dimensions. (a) MTS Layer-I. (b) MTS Layer-II.

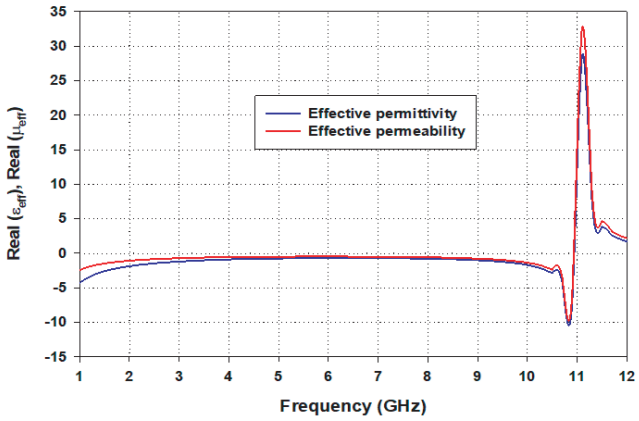

FIGURE 3. Effective permittivity and permeability responses of the proposed MTS structure.

2.2. Design Procedure and Operation

Designing MTS to achieve a multiband response involves the placement of several transmission zeros or 'nulls' at specific frequencies points [5]. Placing the nulls at the appropriate location creates the required passbands between resonant frequencies. To ensure sufficient separation between two passbands, a strong null must be placed, in which there is a significant drop in the transmission efficiency. In the proposed design, the transmission efficiency falls as low as -20 dB (1%) at the nulls. Also, the nulls are stable with respect to incidence angles and polarization. Moreover, the nulls are tuned to achieve the best possible transmission efficiency and bandwidth, without compromising the angular stability. The approach followed in this work is to use different resonant elements and combine their effects by arranging them on the one side of the substrate and cascade with the resonant elements on the other side of the substrate.

The transmission nulls are placed using certain patch-type structures whose frequency response can be predicted using an equivalent circuit model. This reduces the amount of trial and error required in the design process and makes it easier to choose the optimum design dimensions. It is important to note that the behavior of any MTS element is greatly influenced by its location in the unit cell, its surrounding structures, and dielectric properties of the substrate layers. Hence, each element is tested w.r.t the location before including it in the unit cell. This is especially important with respect to angular stability. In order to understand the complete physical impact of unit cell and its associated layers, full-wave method based ANSYS HFSS is used for the EM analysis of proposed structure. The simulation setup along with the boundary condition and excitation is shown in Fig. 4. The combination of master slave boundary conditions is used to define the boundary for the EM simulation, in which the electric field on the slave surface matches the electric field on the master surface within a phase difference. Floquet port is used as excitation type to simulate the EM characteristics of infinitely large proposed metasurface structure, which is used exclusively with planar-periodic structures.

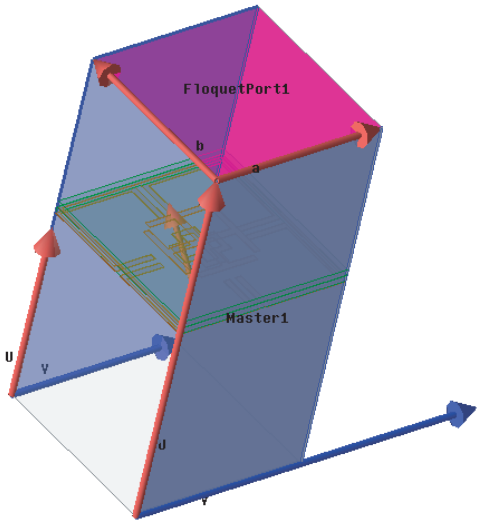

FIGURE 4. Simulation setup for the proposed MTS unit cell in Ansys HFSS V24.R1.

Further, the EM analysis of proposed MTS structure has been performed at normal as well as oblique angle of incidence for TE and TM polarizations as shown in Fig. 5 and Fig. 6, respectively. The results show that the proposed unit cell structure exhibits three passbands with centre frequencies at 3.3 GHz, 4.8 GHz, and 9.1 GHz corresponding to S-, C-, and X-bands, respectively. It is observed that the transmission coefficient of the proposed structure is stable w.r.t angle of incidence (till 60°) in S-, C-, and X-bands. Thus, the proposed metasurface structure shows polarization independent EM characteristics.

Jerusalem cross (JC) is a widely studied FSS structure, known for its angular stability. To create an angular stable multiband transmission characteristic with good isolation between them, two different JC arrays are used to give the nulls at 4.1 GHz and 6.5 GHz. The dimensions are estimated by simulating them separately and then optimized after combining the two. Initially, it was attempted to combine them on a single

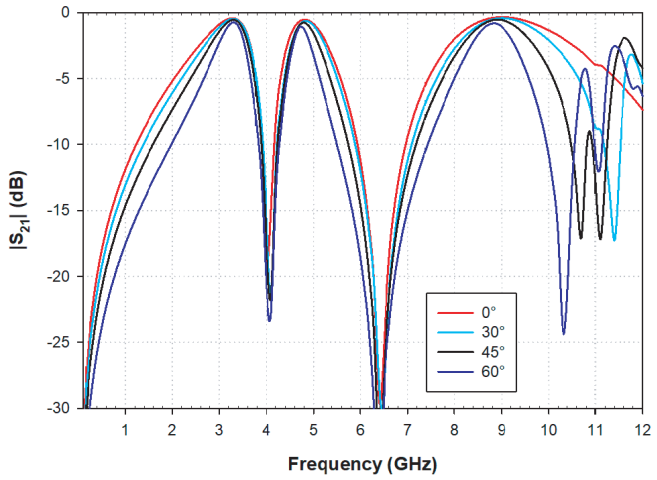

FIGURE 5. Simulated transmission coefficient at different angles of incidence for TE polarization.

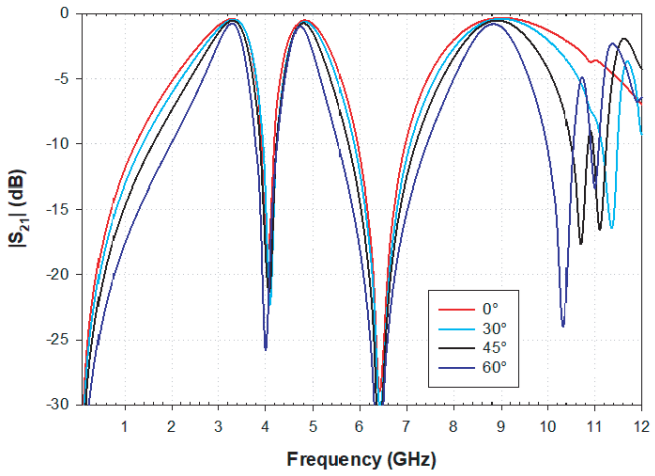

FIGURE 6. Simulated transmission coefficient at different angles of incidence for TM polarization.

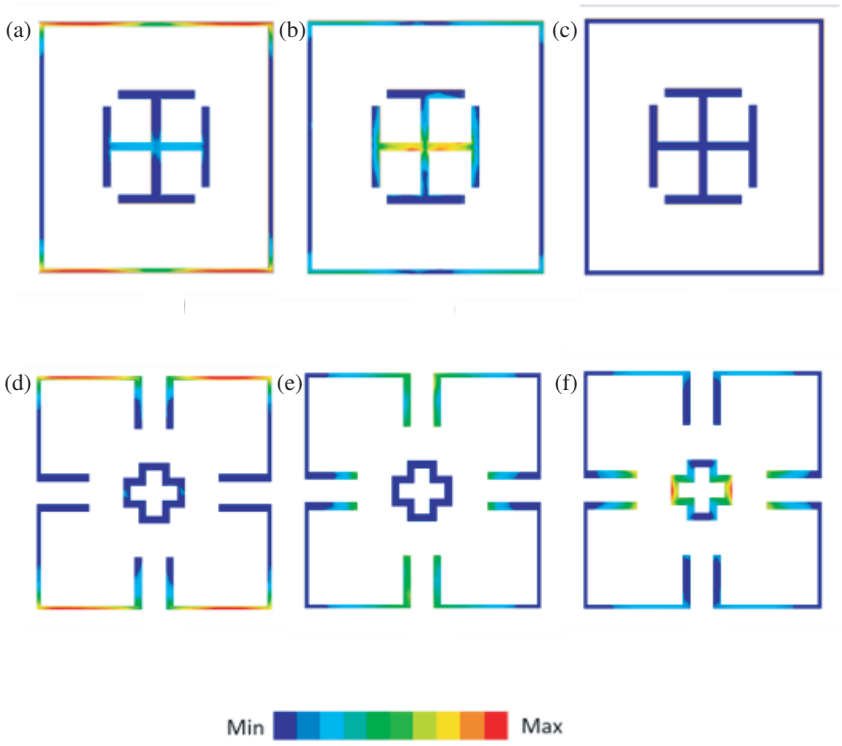

FIGURE 7. Surface current distributions on MTS layer-I: (a) at 3.3 GHz; (b) 4.8 GHz; (c) 9.1 GHz; on MTS layer-II: (d) at 3.3 GHz; (e) at 4.8 GHz; (f) at 9.1 GHz.

MTS layer, but this resulted in an unstable response. Hence, the two JC arrays are cascaded in such a way that they are not cascaded with one directly above the other but are positioned diagonally. This is observed to mitigate the influence of grating lobes, which may be due to reduced broadside coupling effects. The resulting MTS structure is illustrated in Fig. 2 having smaller JC (6.5 GHz) on the upper side and larger JC (4.1 GHz) on the lower side. The larger JC is arranged at the corners of the unit cell. These two elements produce a passband with a center frequency of 4.8 GHz in the C-band, which is clear from the surface current distributions given in Fig. 7(b) and Fig. 7(e).

In order to create the passband at lower frequency, another null is placed at 0.1 GHz using a gridline structure. This structure acts as an inductor and is thus a high-pass filter. The square grid causes some instability due to grating lobes, but the effect is minimized by taking the minimum possible width of the metallic grid. This element has been combined with the smaller JC on the MTS Layer-I to reduce mutual coupling.

The resulting transmission null is observed to be wide, and it creates a passband with a center frequency of 3.3 GHz in the S-band. The surface current distributions on MTS layers-I and -II at 3.3 GHz are given in Fig. 7(a) and Fig. 7(d). Finally, a small cross-shaped loop is added in the MTS Layer-II to introduce a null and suppress the higher order harmonics beyond X-band. This structure is relatively unstable, but it creates a wide passband with a center frequency of 9.1 GHz, in the X-band. At 9.1 GHz, the surface current is more concentrated on the centrally placed cross-shaped loop than other MTS elements in the unit cell (refer Fig. 7(c) and Fig. 7(f)). The simulated transmission coefficient of the proposed MTS structure is represented in Fig. 5 and Fig. 6 for TE and TM polarizations, respectively. With the above mentioned operating principles of MTS structures, the proposed structure could exhibit polarization independence and angular stability till 60°.

Finally, optimization of the dielectric thickness was carried out to maximize the transmission efficiency and bandwidth while keeping the proposed structure suitable for airborne radome applications. To illustrate, parametric analysis of the upper dielectric thickness $h1$ is shown in Fig. 8 at normal incidence. It is observed that increasing dielectric thickness causes an increase in bandwidth and a shift in frequency to lower side. However, it is also seen that the transmission efficiency in the C-band increases while it decreases in the S- and X-bands. Taking into account this tradeoff, as well as certain constraints related to the fabrication, a particular value of dielectric thickness ($h1 = h2 = 0.508$ mm) is selected for each layer.

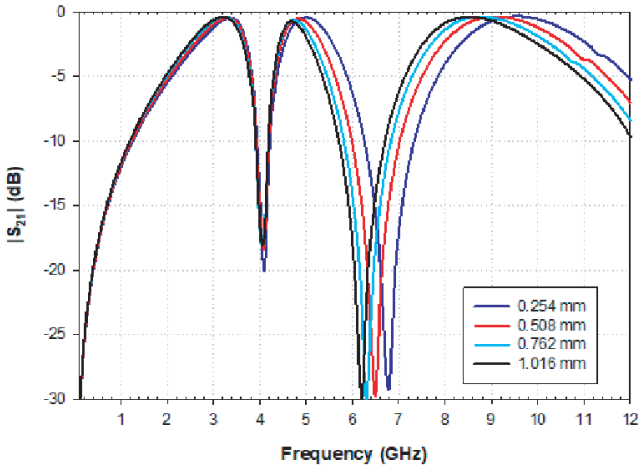

FIGURE 8. Parametric analysis of thickness ($h1$) of upper dielectric layer.

The EM performance analysis of proposed MTS structure is carried out using full-wave method based ANSYS HFSS. The transmission characteristics are studied at normal as well as oblique incidence (till 60°) for both TE and TM polarizations as shown in Fig. 5 and Fig. 6, respectively. It exhibits triple resonances at frequencies 3.3 GHz, 4.8 GHz, and 9.1 GHz, which lie in S-, C-, and X-bands, respectively. Moreover, the transmission response is stable w.r.t the angle of incidence and polarizations that makes the proposed MTS structure for airborne radome covering the shared aperture antenna. Further, it is observed that the proposed MTS structure shows sufficient transmission bandwidth (BW) at its resonance frequencies, 3.3 GHz (BW = 200 MHz), 4.8 GHz (BW = 300 MHz), and 9.1 GHz (BW = 800 MHz) w.r.t −1 dB transmission loss.

3. EQUIVALENT CIRCUIT MODEL OF PROPOSED DESIGN

The equivalent circuit model of the proposed MTS structure is derived as given in Fig. 9 as it consists of two MTS layers viz. MTS Layers-I & -II. The MTS Layer-I comprises a gridded Jerusalem cross (JC), and the MTS Layer-II has the combination of JC positioned at the corners of the unit cell and a cross loop at the center. The outer square grid of the first layer represents an inductive component which is specified by length, p, and width, $w2$, and are responsible for the first null in the S-band and can be calculated as [23],

$$X_{lg} = 4F(p, w_2, \lambda) = \left(\frac{p\cos(\theta)}{\lambda}\right)\left(\ln\left(\frac{\pi w_2}{2p}\right) + G\left(p, w_2, \lambda, \phi\right)\right) \quad (1)$$

where $G(p, w, \lambda, \Phi)$ can be calculated from [24]. JC is a patch type metallic structure, which consists of an inductive reactance and two capacitive susceptances, which are represented by Eqs. (2)–(5), respectively [25],

$$X_{JC1} = \frac{l_2}{p}F\left(p, w_2, \lambda\right) \quad (2)$$

$$X_{JC2} = \frac{l_1}{p}F\left(p, w_1, \lambda\right) \quad (3)$$

$$B_d = 4\frac{2w_t + g_t}{p}F\left(p, p - l_2, \lambda\right) \quad (4)$$

$$B_{gt} = 4\frac{l_2}{p}F\left(p, g_t, \lambda\right) \quad (5)$$

The longer and shorter arms of the JC, having lengths l_1 and l_2 and width w_1, contribute to the inductive component of the JC. In Eqs. (4)–(5), g_t is the gap between adjacent JCs. The capacitive components arise from the gaps between the adjacent JCs in the MTS array. Due to the discontinuity of the structure

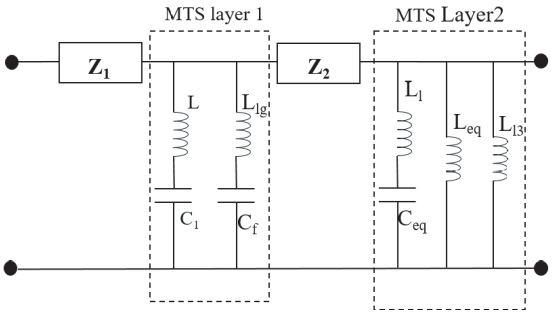

FIGURE 9. Equivalent circuit model of proposed MTS structure.

in the array, reduction factors $\frac{l_2}{p}$ and $\frac{2w_1+g_t}{p}$ appear in the relation. Apart from the inductive and capacitive reactance components, fringe capacitance at the outer edge of the metallic strip should also be considered while calculating the total admittance of the top MTS layer of the proposed structure [26]. This contributes to the bandwidth of the S-band transmission response and can be calculated from the following expression,

$$C_f = \frac{1}{2}\left(\frac{\sqrt{\epsilon_r}}{cZ} - \frac{\sqrt{\epsilon_r}\sqrt{\epsilon_0}w_1}{h_{re}}\lambda\right) \tag{6}$$

where h_{re} is the dielectric thickness; w_1 is the width of the strip; and Z can be calculated as [15],

$$Z = \frac{\eta}{2\pi\sqrt{\epsilon_{re}}}\ln\left(\frac{8h}{w_1} + 0.25\frac{w_1}{h}\right) \tag{7}$$

Finally, the admittance of the gridded JC (GJC) is calculated by,

$$Y_1 = j\frac{2\left(\frac{B_1}{1-XB_1} + 2\left(\frac{B_f}{1-X_{lg}B_f}\right)\right)}{Z_0} \tag{8}$$

where $B_f = \omega C_f$, X is the equivalent inductive reactance of X_{JC1} and X_{JC2}, and B_1 is the sum of capacitive susceptance of B_{d1} and B_{g1}. These series LC resonant circuits control the second transmission null in the C-band. The factor 2 in Eq. (8) appears due to the repetition of the inductive and capacitive components in the unit cell. Z_0 represents the free-space impedance.

The MTS layer-II of the radome structure comprises a cross loop and part of JC positioned at the corners of each unit cell, which will result in a whole JC in the array. This JC is also modelled with the same equivalent circuit but different parameters, since the size of the JC is different from those at the first layer. Here, the lengths of the arms of the JC are equal. So, the corresponding inductive component is given by Eq. (9),

$$X_{JC1} = \frac{l_3}{p}F\left(p, w_4, \lambda\right) \tag{9}$$

Rest of the susceptive components are given by Eqs. (10)–(13),

$$B_d = 4\frac{2w_3+g}{p}F\left(p, p-l_3, \lambda\right) \tag{10}$$

$$B_{g1} = 4\frac{l_3}{p}F\left(p, g, \lambda\right) \tag{11}$$

$$C_{f1} = \frac{1}{2}\left(\frac{\sqrt{\epsilon_r}}{cZ} - \frac{\sqrt{\epsilon_r}\sqrt{\epsilon_0}w_3}{h_{re1}}\lambda\right) \tag{12}$$

$$B_{f1} = \omega C_{f1} \tag{13}$$

Two series LC circuits in parallel represent the equivalent circuit of the cross-loop of the second layer [27]. The geometrical parameters of the cross loop are given as l_6, l_7, g_1, g_2, and w_5, where l_6, l_7 are the lengths of the cross dipole; g_1, g_2 are the gaps at the centre and sides of the cross dipole, respectively; and w_5 is the width of the cross-shaped loop. The reactive components of the cross loop are given by Eqs. (14)–(16) as,

$$B_{g1} = 4\frac{2l_6}{p}F\left(p, g_1, \lambda\right) \tag{14}$$

$$X_{l1} = \frac{l_6}{p}F\left(p, w_5, \lambda\right) \tag{15}$$

Now, the equivalent reactance of the above components is given by,

$$X_1 = 2\frac{B_{c1}}{1 - X_{l1}B_{c1}} \tag{16}$$

Similarly, we can obtain B_{c2}, X_{l2}, X_2, and X_{l3} from above equations. Now, the admittance of the MTS layer-2 is calculated from Eq. (17) as,

$$Y_2 = j\frac{2\left(\frac{B_{eq}}{1-2X_lB_{eq}} + \left(\frac{X_{eq}X_{l3}}{X_{eq}+X_{l3}}\right)\right)}{Z_0} \tag{17}$$

where B_{eq} is the equivalent capacitive susceptance of B_{g1}, B_{f1}, and B_d, and it controls the third transmission null in the C-band. X_{eq} is the equivalent inductive reactance of X_1 and X_2, and it controls the fourth transmission null in the X-band. Also, the two parallel inductive reactances, X_{eq} and X_{l3} together control the transmission pole in the X-band. Once the equivalent circuit modelling of the proposed design has been completed, the transmission coefficient can be calculated using conventional transmission line theory [7] as,

$$S_{21} = \frac{2}{A + \left(\frac{B}{Z_0}\right) + CZ_0 + D} \tag{18}$$

where A, B, C, D represent the $ABCD$ matrix system composed of the MTS and dielectrics. Here, the matrix can be defined as follows,

$$\begin{bmatrix} A & B \\ C & D \end{bmatrix} = \left[M_1\right]\left[M_{MTS1}\right]\left[M_2\right]\left[M_{MTS2}\right] \tag{19}$$

In Eq. (19), subscripts 1, 2, $MTS1$, and $MTS2$ represent the upper dielectric substrate, lower dielectric substrate, top MTS layer, and bottom MTS layer, respectively. In general, scattering matrix of the dielectric layer can be obtained by Eq. (20) as,

$$\left[M\right] = \begin{bmatrix} \cos\phi & j\frac{Z_0}{\sqrt{\epsilon_r - sin^2\theta}}\sin\phi \\ j\frac{\sqrt{\epsilon_r - \sin^2\theta}}{Z_0}\sin\phi & \cos\phi \end{bmatrix} \tag{20}$$

where ϕ is the electrical length in radians and is given by,

$$\phi = \frac{2\pi h\sqrt{\epsilon_r - \sin^2\theta}}{\lambda} \tag{21}$$

The term h in the above equation represents the height of the dielectric layer. ϵ_r represents the relative permittivity, θ the

angle of incidence, and λ the free-space wavelength. Now the matrix corresponding to the MTS layer is given by,

$$[M_{FSS}] = \begin{bmatrix} 1 & 0 \\ Y_{FSS} & 0 \end{bmatrix} \tag{22}$$

Y_{FSS} is the total admittance offered by MTS layers 1 & 2. By substituting the values of matrices M_1, M_2, M_{MTS1}, and M_{MTS2}, the transmission coefficient of the proposed MTS structure can be calculated using Eq. (18). Fig. 10 shows the predicted result from the equivalent circuit model and its validation with simulated results based on HFSS. The predicted result based on ECM is found in good agreement with the simulated (HFSS) results. The slight shift in transmission nulls around 12 GHz is observed which may be due to the different theoretical approaches used to obtain the transmission response of the proposed multiband MTS structure.

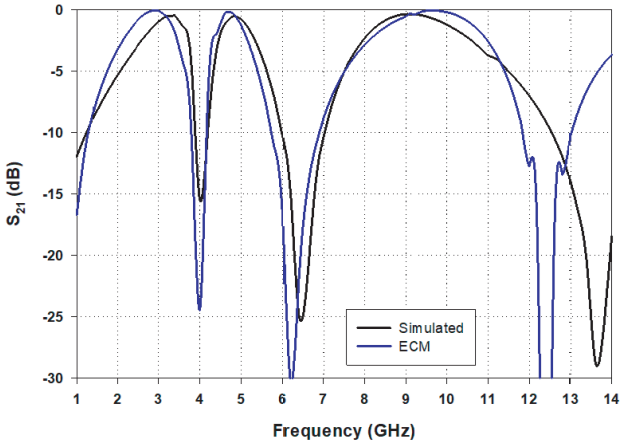

FIGURE 10. Comparison between HFSS simulated and predicted result by the equivalent circuit model of the proposed multiband MTS structure.

4. EXPERIMENTAL VERIFICATION

In order to verify the validity of simulated results and for proof-of-the-concept, a prototype (size: 300 mm × 300 mm × 1.016 mm) has been fabricated (Fig. 11) and tested in an anechoic chamber using free-space method. The transmission loss of fabricated planar MTS structure was measured at normal incidence and compared with that of simulated results as shown in Fig. 12. Excellent matching was obtained between measured and simulated results except lower frequency side from 1 to 2.8 GHz due to functional constraints of anechoic chamber below 2 GHz. Moreover, results based on ECM have also been validated with measured result. Thus, the predicted result is observed to closely match the measured ones except at higher frequency side from 11 to 14 GHz.

5. EM ANALYSIS OF MTS BASED MULTILAYERED PLANAR LAMINATE

In view of airborne radome applications, an MTS based multilayered planar laminate is designed employing the proposed

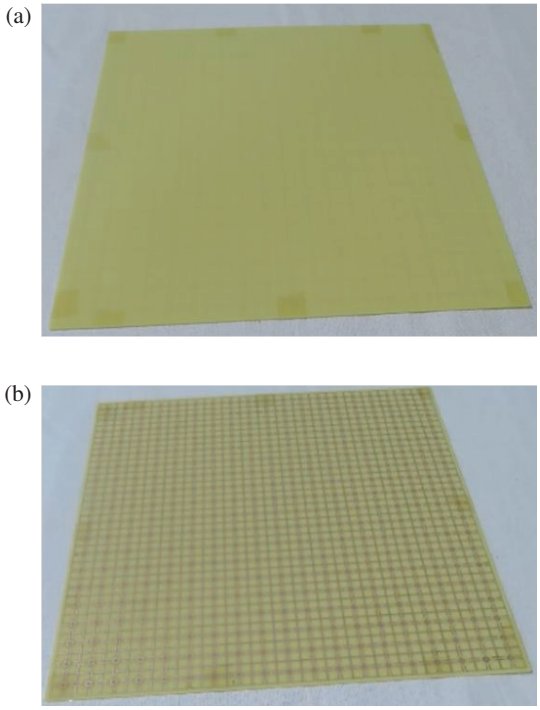

FIGURE 11. A prototype of proposed MTS structure with top and bottom view (size: 300 mm × 300 mm × 1.016 mm); (a) Top view. (b) Bottom view.

MTS structure (Fig. 13). The proposed multilayered MTS planar laminate comprises seven layers including the proposed MTS structure as the middle layer. The inner and outer skin layers are made of Glass Epoxy. The inner and outer core layers comprise Rohacell foam material ($\epsilon_r = 1.05$ and $\tan\delta = 0.0027$) of thickness 2.5 mm. The thickness of outer and inner skins is optimized to be 0.508 mm, while thickness of the middle layer is optimized to be 1.016 mm. Incorporating foam material enhances the overall strength of the design without having much impact on the transmission efficiency of incident electromagnetic waves. The mechanical properties of raw materials (Rohacell Foam and Glass Epoxy) used for designing the MTS based multilayered composite laminate are listed in Table 2. In view of designing multilayered planar laminate, the periodicity of the MTS structure has been optimized to be 14.5 mm. The length and width of the arms of the JC in the MTS layer-I have been modified to 5.5 mm and 0.6 mm, respectively, to obtain stable performance over the higher angles of incidence. The rest of the MTS parameters are considered to be the same as those given in Table 1.

The transmission and reflection characteristics of the proposed MTS based multilayered planar laminate are shown in Fig. 14 and Fig. 15, respectively for both TE and TM polarizations. The multilayered radome is observed to resonate at frequencies 2.5 GHz (in S-band), 5.1 GHz (in C-band), and 9.8 GHz (in X-band). The proposed configuration demonstrates stable performance up to 60° of oblique incidence for both TE and TM polarizations. Additionally, it exhibits the transmission bandwidth of 220 MHz, 1 GHz, and 1.3 GHz in S-, C-, and X-bands, respectively, w.r.t −1 dB insertion loss. In view of practical applications, the insertion phase delay (IPD) for the

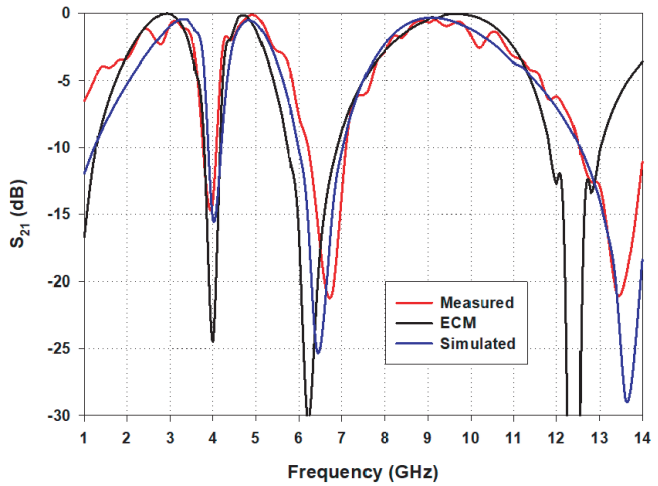

FIGURE 12. Validation of simulated (HFSS) and predicted (ECM) transmission responses with the measured result at normal incidence.

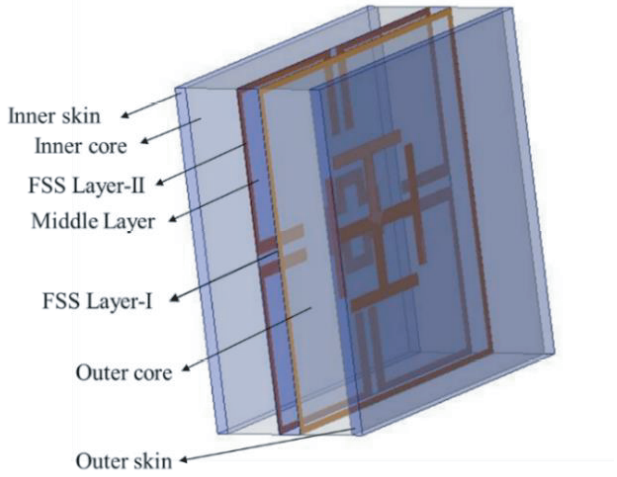

FIGURE 13. Schematic of MTS based multilayered planar laminate.

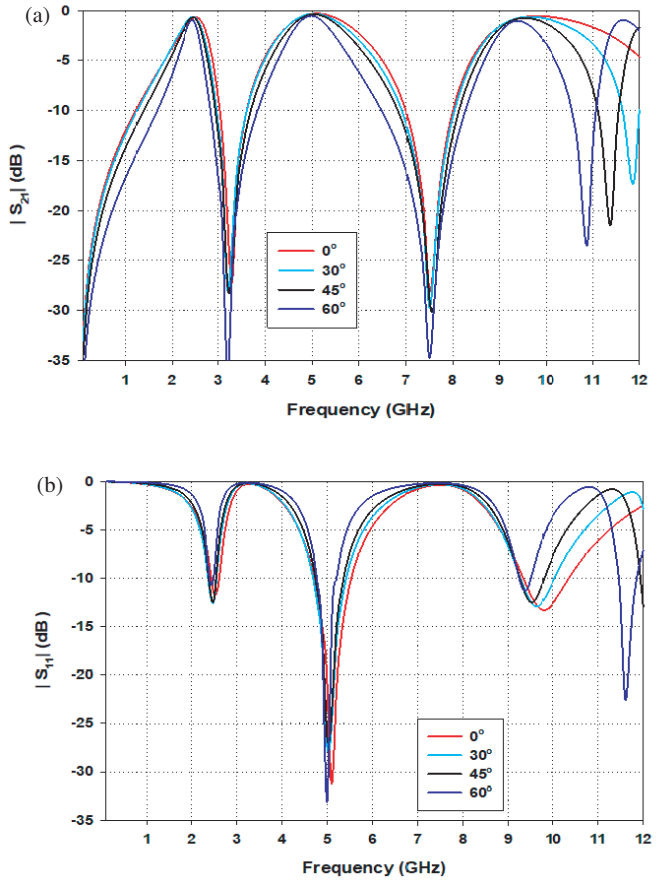

FIGURE 14. Simulated EM characteristics of MTS based multilayered planar laminate configuration at different angles of incidence for TE polarization; (a) transmission coefficient, (b) reflection coefficient.

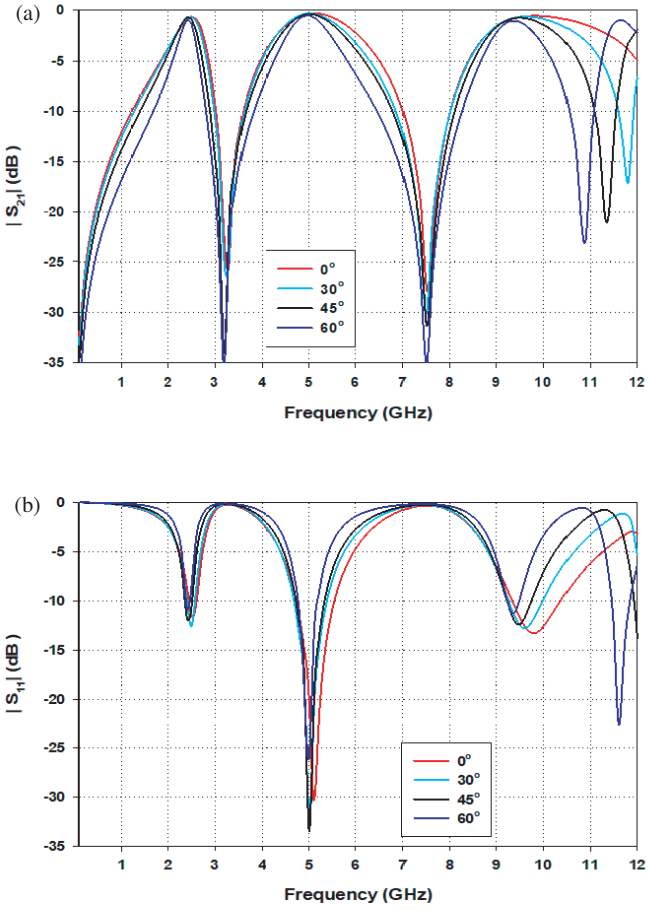

FIGURE 15. Simulated EM characteristics of MTS based multilayered planar laminate at different angles of incidence for TM polarization; (a) transmission coefficient, (b) reflection coefficient.

MTS based multi-layered radome configuration has been calculated by [28],

$$IPD = -(\angle T_1 + \angle T_2 + \ldots + \angle T_N)) \quad -2\pi \sum_{i=1}^{n} \left(\frac{d_i}{\lambda_i}\right) \cos\theta_i \tag{23}$$

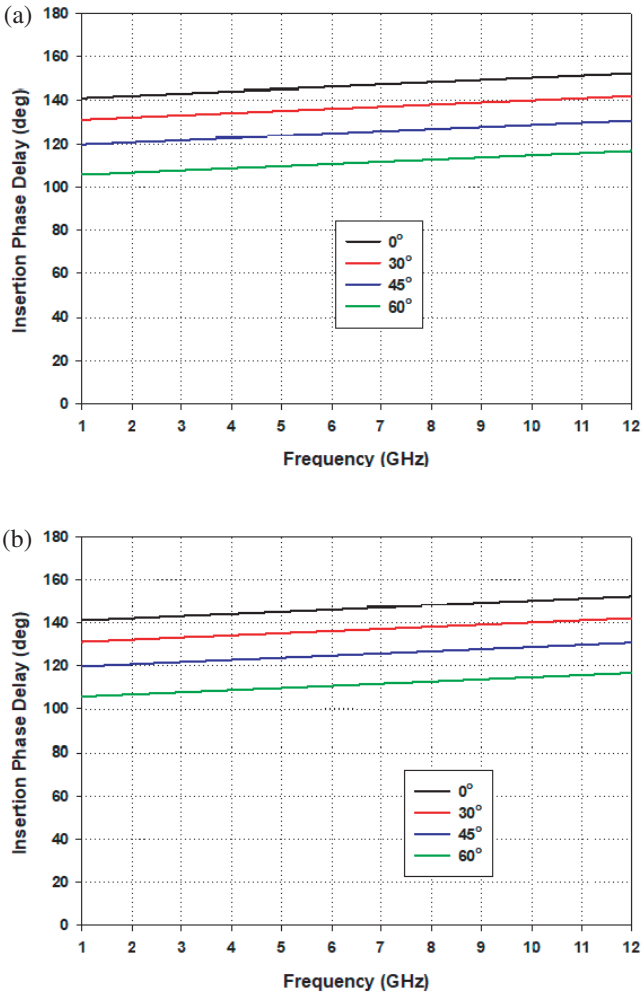

FIGURE 16. Insertion phase delay of MTS based multilayered radome at incidence angles 0°, 30°, 45°, and 60° for (a) TE polarization, (b) TM polarization.

where d_i and λ_i are the thickness and wavelength in each layer, respectively. θ_i is the angle of incidence at each layer. IPD of the multi-layered planar laminate configuration has been studied w.r.t frequency for different angles of incidence for TE and TM polarizations (see Fig. 16). It is observed that IPD is stable over the desired frequency range at different angles of incidence for both polarizations.

6. STRUCTURAL ANALYSIS OF MTS BASED MULTI-LAYERED RADOME

The structural integrity of a radome is equally important as its electromagnetic performance. Radome must satisfy both EM and structural requirements. Electromagnetically, airborne radomes should demonstrate low transmission loss, polarization insensitivity, stable performance at high incidence angles, and minimal aberration. Structurally, the primary consideration in radome design is ensuring that it can withstand against necessary loads under specific conditions. The proposed MTS based multi-layered radome is intended to use in the leading wing edge of the aircraft. For the structural analysis, a CAD model of the wing structure has been created in CATIA V5, comprosed of MTS based multi-layered configuration (see Fig. 17) and mechanical properties of Glass epoxy, and Rohacell foam is considered as per Table 2. A typical cross-section of a leading edge wing structure has been selected for the structural analysis, with the wing edges constrained as illustrated in Fig. 17 to mark the boundary conditions. In the analysis process, the entire structure is divided into individual mesh units, which are in the shapes of quads and trias with a size of 1 mm. In view of aerospace applications, a pressure force of 10 KPa is uniformly applied over the structure for the analysis, and the resulting deformation caused by this load has been calculated [29, 30].

TABLE 2. Mechanical properties of rohacell foam and glass epoxy used for designing MTS based multi-layered laminate.

Material	Properties	Values (Unit)
ROHACELL 51 R Foam	Tensile strength	1.6 MPa
	Compressive strength	0.8 MPa
	Shear Strength	0.8 MPa
	Elastic Modulus	75 MPa
	Shear Modulus	24 MPa
	Density	52 kg/m^3
	Poisson's Ratio	0.38
Glass Epoxy	Longitudinal tensile modulus	22 GPa
	Transverse tensile modulus	21 GPa
	Poisson's Ratio	0.17
	Shear modulus	4 GPa
	Density	1.75 gm/cc
	Longitudinal tensile strength	380 MPa
	Longitudinal compression strength	360 MPa
	Transverse tensile strength	360 MPa
	Transverse compression strength	340 MPa
	Inter laminar shear strength	40 MPa

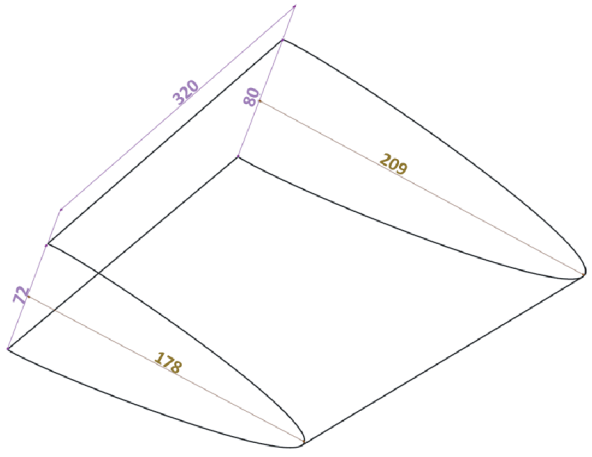

FIGURE 17. CAD model of the leading wing structure of the aircraft (all the dimensions are in mm).

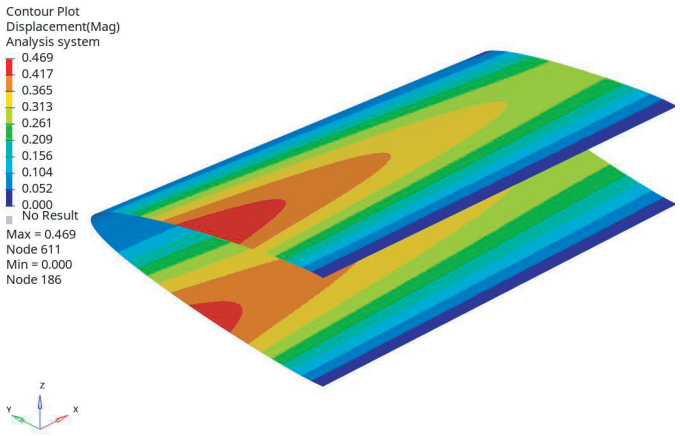

FIGURE 18. Total deflection on the wing structure.

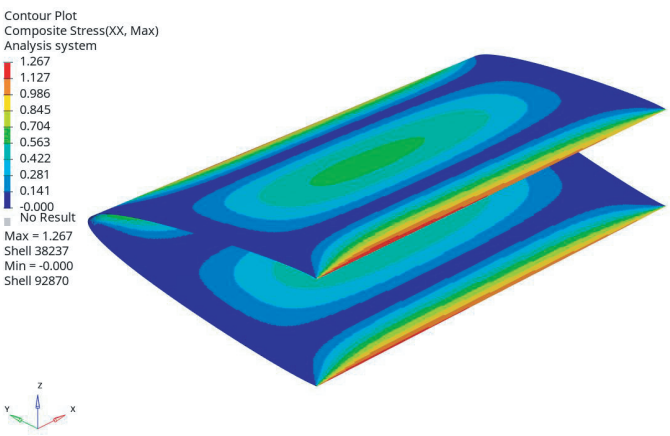

FIGURE 19. Normal stress along lateral direction.

TABLE 3. EM performance comparison between proposed MTS design and reported designs.

Ref. No.	Operating Frequencies (GHz)	Angular stability	Substrate thickness (mm)	Periodicity (mm)	−3 dB Fractional bandwidth (%)	Polarization insensitive
[31]	2.4, 3.5, 5.5	60°	1.6	20 × 20	-	No
[32]	2.68, 6.88, 10.51	60°	1.6	20 × 20	35.87, 11.86, 19.28	Yes
[33]	2.55, 4.26	45°	2.4	16 × 16	1.18, 21.04	Yes
[34]	7.0, 10.9, 11.8	45°	1.2	12 × 12	-	No
[35]	2.4, 3.5, 5.8	45°	1.57	12 × 12	23.26, 16.76	No
This work	**3.3, 4.8, 9.1**	**60°**	**1.016**	**15.5 × 15.5**	**37, 21.25, 33.52**	Yes

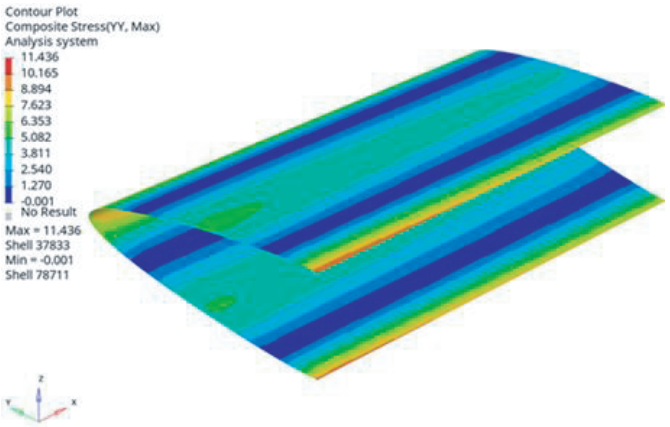

FIGURE 20. Normal stress along longitudinal direction.

Figure 18 indicates that the maximum deformation caused by this load is 0.47 mm. The maximum normal stress along the lateral and longitudinal directions is observed to be 1.276 MPa and 11.46 MPa, respectively (see Fig. 19 and Fig. 20), which are less than the maximum allowable strength of the material. Hence, the radome structure is safe for the applied load with sufficient margin.

7. CONCLUSION

In this paper, a novel angular stable and polarization independent metasurface-based structure has been presented, which exhibits multiband operation at frequencies 3.3 GHz, 4.8 GHz, and 9.1 GHz with very good isolation (< -20 dB) between the bands. For proof-of-the concept, a prototype planar metasurface structure was fabricated and tested in an anechoic chamber. The overall thickness of the proposed multiband metasurface structure is 1.016 mm ($\lambda/30$ w.r.t highest operating frequency), which is significantly less than the existing multiband radome designs in the open domain. Table 3 presents a comparison of EM performance of the proposed triple bandpass MTS design with other existing designs in open literature. As compared to [32] that exhibits similar frequency bands, the proposed metasurface structure exhibits wider fractional bandwidth (w.r.t −3 dB transmission loss) and has lesser substrate thickness. Further, a multilayered planar laminate was designed using the proposed metasurface in view of application to the shared aperture antenna installed at leading wing edge of the aircraft. The structural analysis of multilayered radome wall configuration confirmed its suitability.

ACKNOWLEDGEMENT

Author, Ms. Arya K M, is grateful to the Department of Science and Technology (DST), India, for the financial support under the INSPIRE FELLOWSHIP program.

REFERENCES

[1] Chakrabarti, S., E. N. Das, and G. Barman, "A shared aperture microstrip antenna for S/C-band communications," *International Journal of System Assurance Engineering and Management*, Vol. 14, No. Suppl 2, 595–602, 2023.

[2] Narayan, S. and R. M. Jha, "Electromagnetic techniques and design strategies for FSS structure applications [antenna applications corner]," *IEEE Antennas and Propagation Magazine*, Vol. 57, No. 5, 135–158, 2015.

[3] Parker, E. A., "The gentleman's guide to frequency selective surfaces," in *17th Q.M.W. Antenna Symposium*, London, UK, Apr. 1991.

[4] Guo, C., H.-J. Sun, and X. Lv, "A novel dualband frequency selective surface with periodic cell perturbation," *Progress In Electromagnetics Research B*, Vol. 9, 137–149, 2008.

[5] Li, B. and Z. Shen, "Synthesis of quasi-elliptic bandpass frequency-selective surface using cascaded loop arrays," *IEEE Transactions on Antennas and Propagation*, Vol. 61, No. 6, 3053–3059, 2013.

[6] Li, M. and N. Behdad, "A third-order bandpass frequency selective surface with a tunable transmission null," *IEEE Transactions on Antennas and Propagation*, Vol. 60, No. 4, 2109–2113, 2012.

[7] Li, W. and Y. Li, "A high selectivity, miniaturized, low profile dual-band bandpass FSS with a controllable transmission zero," *International Journal of Antennas and Propagation*, Vol. 2017, No. 1, 7983567, 2017.

[8] Liu, N., X. Sheng, C. Zhang, and D. Guo, "Design of dual-band composite radome wall with high angular stability using frequency selective surface," *IEEE Access*, Vol. 7, 123 393–123 401, 2019.

[9] Xu, G., S. V. Hum, and G. V. Eleftheriades, "A technique for designing multilayer multistopband frequency selective surfaces," *IEEE Transactions on Antennas and Propagation*, Vol. 66, No. 2, 780–789, 2017.

[10] Wang, D., W. Che, Y. Chang, K.-S. Chin, and Y.-L. Chow, "Combined-element frequency selective surfaces with multiple transmission poles and zeros," *IET Microwaves, Antennas & Propagation*, Vol. 8, No. 3, 186–193, 2014.

[11] Zhang, J.-C., Y.-Z. Yin, and J.-P. Ma, "Frequency selective surfaces with fractal four legged elements," *Progress In Electromagnetics Research Letters*, Vol. 8, 1–8, 2009.

[12] Li, Z., J. Dong, and J. Mo, "A miniaturized quad-band frequency selective surface," in *2020 Cross Strait Radio Science & Wireless Technology Conference (CSRSWTC)*, 1–3, Fuzhou, China, Dec. 2020.

[13] Prasad, P. and A. Kumar, "A miniaturized quintuple-band frequency selective surface based on enclosed cross slots," *Journal of Electrical Engineering*, Vol. 74, No. 4, 293–301, 2023.

[14] Öziş, E., A. V. Osipov, and T. F. Eibert, "Metamaterials for microwave radomes and the concept of a metaradome: Review of the literature," *International Journal of Antennas and Propagation*, Vol. 2017, No. 1, 1356108, 2017.

[15] Wang, S., H.-X. Xu, M. Wang, H. Wei, F. Zhang, and G. Hu, "Janus metasurface for super radome with asymmetric diffusion and absorption," *Advanced Optical Materials*, Vol. 12, No. 7, 2302061, 2024.

[16] Su, H.-L., H.-C. Huang, K.-H. Lin, C.-Y. Wu, and H.-H. Lin, "Gain-enhanced metamaterial radome for circularly-polarized antenna," in *2010 IEEE Antennas and Propagation Society International Symposium*, 1–4, Toronto, ON, Canada, Jul. 2010.

[17] Mirzapour, M. I., A. Ghorbani, and F. A. Namin, "Metasurface radome to achieve a wideband high gain, low RCS, and low SLL antenna," *IETE Journal of Research*, Vol. 70, No. 1, 206–213, 2024.

[18] Pang, X., T. Zhang, M. Hu, H. Zhang, and Q. Zheng, "Broadband low-scattering and high-efficiency transmission radome by combining phase gradient metasurface and FSS," *Optics Communications*, Vol. 563, 130598, 2024.

[19] He, Y. and G. V. Eleftheriades, "A thin double-mesh metamaterial radome for wide-angle and broadband applications at millimeter-wave frequencies," *IEEE Transactions on Antennas and Propagation*, Vol. 68, No. 3, 2176–2185, 2019.

[20] Narayan, S., G. Gulati, B. Sangeetha, and R. U. Nair, "Novel metamaterial-element-based FSS for airborne radome applications," *IEEE Transactions on Antennas and Propagation*, Vol. 66, No. 9, 4695–4707, 2018.

[21] Aserkar, A. M., K. M. Arya, D. Joseph, R. U. Nair, and S. Narayan, "Design of multiband FSS-radome for shared aperture antenna application," in *2023 IEEE Microwaves, Antennas, and Propagation Conference (MAPCON)*, 1–4, Ahmedabad, India, Dec. 2023.

[22] Chen, X., T. M. Grzegorczyk, B.-I. Wu, J. P. Jr., and J. A. Kong, "Robust method to retrieve the constitutive effective parameters of metamaterials," *Physical Review E — Statistical, Nonlinear, and Soft Matter Physics*, Vol. 70, No. 1, 016608, 2004.

[23] Szabó, Z., G.-H. Park, R. Hedge, and E.-P. Li, "A unique extraction of metamaterial parameters based on Kramers–Kronig relationship," *IEEE Transactions on Microwave Theory and Techniques*, Vol. 58, No. 10, 2646–2653, 2010.

[24] Lee, C. K. and R. J. Langley, "Equivalent-circuit models for frequency-selective surfaces at oblique angles of incidence," in *IEE Proceedings H (Microwaves, Antennas and Propagation)*, Vol. 132, No. 6, 395–399, 1985.

[25] Li, T.-W., Y.-D. Fan, Y.-J. Gu, S.-Y. Zhou, P.-F. Qin, D. Li, W. E. I. Sha, and E.-P. Li, "A novel miniaturized multiband strong coupled-FSS structure insensitive to almost all angles and all polarizations," *IEEE Transactions on Antennas and Propagation*, Vol. 69, No. 12, 8470–8478, 2021.

[26] Langley, R. J. and E. A. Parker, "Equivalent circuit model for arrays of square loops," *Electronics Letters*, Vol. 18, 294–296, 1982.

[27] Hosseinipanah, M. and Q. Wu, "Equivalent circuit model for designing of Jerusalem cross-based artificial magnetic conductors," *Radioengineering*, Vol. 18, No. 4, 544–550, 2009.

[28] Narayan, S., S. B. Joshi, R. U. Nair, and R. M. Jha, "Electromagnetic performance analysis of novel multi-band metamaterial FSS for millimeter wave radome applications," *Computers Materials and Continua*, Vol. 31, No. 1, 1, 2012.

[29] Steffen, O., P. Meyer, and C. Hühne, "Natural laminar flow leading edge: Requirements, design, and experimental validation under operational loads," *Aerospace Science and Technology*, Vol. 146, 108913, 2024.

[30] Hürlimann, F., R. Kelm, M. Dugas, and G. Kress, "Investigation of local load introduction methods in aircraft pre-design," *Aerospace Science and Technology*, Vol. 21, No. 1, 31–40, 2012.

[31] Noor, D., S. K. Yadav, and S. Yadav, "A triple bandpass frequency selective surface for enhancement in the transmission of WiMax and WLAN application," in *2017 International Conference on Computer, Communications and Electron-*

ics (Comptelix), 211–215, Jaipur, India, Aug. 2017.

[32] Kumar, R., A. Rajput, K. Saurav, and S. K. Koul, "A triple band-pass polarization insensitive and angular stable frequency selective surface," in *2021 IEEE MTT-S International Microwave and RF Conference (IMARC)*, 1–4, Kanpur, India, Dec. 2021.

[33] Han, J. and R. Chen, "Dual-band metasurface for broadband asymmetric transmission with high efficiency," *Journal of Applied Physics*, Vol. 130, No. 3, 2021.

[34] Gao, C., H. Pu, S. Gao, C. Chen, and Y. Yang, "Design and analysis of a tri-band frequency selective surface with a second-order response," *International Journal of Microwave and Wireless Technologies*, Vol. 12, No. 3, 205–211, 2020.

[35] Flávio, H. C. S. F., J. P. L. Araújo, A. G. Neto, I. B. G. Coutinho, F. J. B. Barros, G. P. S. Cavalcante, and M. C. d. A. Neto, "Tri-band, stable and compact patch frequency selective surface optimized via hybrid bioinspired computing for applications at 2.4, 3.5 and 5.8 GHz," *Journal of Microwaves, Optoelectronics and Electromagnetic Applications*, Vol. 20, No. 3, 570–584, 2021.